

THE ABUNDANCE GRADIENT IN THE EXTREMELY FAINT OUTER DISK OF NGC 300

M. VLAJIĆ¹, J. BLAND-HAWTHORN², AND K. C. FREEMAN³

¹ Astrophysics, Department of Physics, Keble Road, University of Oxford, Oxford OX1 3RH, UK; vlajic@astro.ox.ac.uk

² Institute of Astronomy, School of Physics, University of Sydney, NSW 2006, Australia

³ Mount Stromlo Observatory, Private Bag, Woden, ACT 2611, Australia

Received 2008 July 10; accepted 2009 March 5; published 2009 May 1

ABSTRACT

In an earlier work, we showed for the first time that the resolved stellar disk of NGC 300 is very extended with no evidence for truncation, a phenomenon that has since been observed in other disk galaxies. We revisit the outer disk of NGC 300 in order to determine the metallicity of the faint stellar population. With the Gemini Multi Object Spectrograph camera at Gemini South, we reach 50% completeness at $(g', i') = (26.8\text{--}27.4, 26.1\text{--}27.0)$ in photometric conditions and $0''.7$ seeing. At these faint depths, careful consideration must be given to the background galaxy population. The mean colors of the outer disk stars fall within the spread of colors for the background galaxies, but the stellar density dominates the background galaxies by $\sim 2 : 1$. The predominantly old stellar population in the outer disk exhibits a negative abundance gradient—as expected from models of galaxy evolution—out to about 10 kpc where the abundance trend changes sign. We present two scenarios to explain the flattening, or upturn, in the metallicity gradient of NGC 300 and discuss the implication this has for the broader picture of galaxy formation.

Key words: galaxies: abundances – galaxies: individual (NGC 300) – galaxies: stellar content – galaxies: structure

1. INTRODUCTION

Simulations of galaxy formation in cosmological context reveal that the process of galaxy assembly is expected to leave an imprint on the characteristics of stars in the faint outer regions of disk galaxies (Bullock & Johnston 2005). Due to their long dynamical timescales, these regions retain the fossil record from the epoch of galaxy formation in the form of spatial and kinematic distributions, ages, and chemical abundances of their stars (Freeman & Bland-Hawthorn 2002). These are also the regions where the effects of stellar radial mixing are expected to be most prominent (Roškar et al. 2008a; Schoenrich & Binney 2008). The structure of the outer parts of galactic disks is therefore central to our understanding of the formation and evolution of disk galaxies.

The studies of galactic disks have identified three basic classes of surface brightness profiles in galaxies (Pohlen et al. 2008). Truncations in surface brightness profiles, characterized by the smooth break between the inner shallower and the outer steeper exponential, have been known for more than two decades and detected in a large number of galaxies (van der Kruit 1979; de Grijs et al. 2001; Pohlen et al. 2002). Despite this, the origin of the break remains unclear. The currently favored model for the explanation of these “subexponential” truncations is the star formation threshold scenario (Kennicutt 1989; Schaye 2004; Roškar et al. 2008a; but see van der Kruit 2007). The threshold gas densities predicted in these models ($3\text{--}10 M_{\odot} \text{ pc}^{-2}$; Schaye 2004) broadly agree with the observed surface brightnesses at the radius of the break which correspond to stellar mass densities of $10\text{--}22 M_{\odot} \text{ pc}^{-2}$ (Bakos et al. 2008). The second class of surface brightness profiles, so-called “upbending” or “superexponential” breaks, have been explained by a scenario involving minor mergers, supported both observationally (Ibata et al. 2005) and by N -body/smoothed particle hydrodynamics simulations (Younger et al. 2007). Until recently, it was believed that all galaxy disks undergo truncation near the Holmberg radius ($26.5 \text{ mag arcsec}^{-2}$) and that this was telling us something important about the collapsing protocloud of gas that formed the early disk (van der Kruit 1979). This

picture was challenged by our earlier finding (Bland-Hawthorn et al. 2005) of a classic exponential disk (Freeman 1970) with no break in NGC 300, out to the distances corresponding to 10 disk scale lengths in this low-luminosity late-type spiral.

The existence of stars at such low stellar surface densities ($0.01 M_{\odot} \text{ pc}^{-2}$; Bland-Hawthorn et al. 2005) in the outer spiral disk has provided the motivation for this work. We seek to learn which physical process are responsible for the formation of the outer disks, and what the nature of the stellar populations in this rarefied medium is. To this end, we obtained additional multiband photometry (g', i') with Gemini/GMOS which allowed us to explore ages and metallicities of the stars in the outer regions of NGC 300.

A number of studies have addressed the question of star formation in outer galactic disks. Davidge (2003, 2006, 2007) find young and intermediate-age stars at large galactocentric distances in NGC 2403, NGC 247, and M33. Barker et al. (2007) discovered young (less than 500 Myr old) main-sequence (MS) stars in the outer regions of M33, beyond the break radius at 4.5 scale lengths (Ferguson et al. 2007). The existence of stars less than 0.5 Gyr old would suggest a very recent star formation episode in the outer disk of M33 as there probably has not been sufficient time for these stars to be scattered from the inner disk and migrate outward. The same study also finds that the scale lengths of stellar populations in M33 increase with age. This is in contrast to the common scenario of inside-out galaxy formation in which the scale length of stars increase as the disks builds up to its present size, and it is expected that the mean age of the stellar disk decreases with radius (Larson 1976; Matteucci & Francois 1989; Chiappini et al. 1997; Naab & Ostriker 2006; Muñoz-Mateos et al. 2007). These findings emphasize how little is understood about the formation of outer disks of spirals and call for deep photometric data on more pure disk galaxies.

The Sculptor Group of galaxies, of which NGC 300 is a member, is one of the nearest and largest ensembles of disk galaxies outside the Local Group. Its galaxies are believed to be more or less isolated and as such are an ideal sample for our proposed study. NGC 300 is an almost pure disk galaxy (bulge light $< 2\%$), with mild inclination ($i = 42^\circ$), which

Table 1
GMOS Observing Log

Target	R.A. (J2000)	Decl. (J2000)	Date	Filter	Exposure (s)	FWHM (")
NGC 300 1	0 55 50	−37 47 18	2005 Sep 7–8	g'	13 × 600	0.71
...	0 55 50	−37 47 24	2005 Aug 4	i'	22 × 600	0.66
NGC 300 2	0 56 15	−37 46 45	2005 Aug 8–10	g'	13 × 600	0.72
...	0 56 15	−37 46 45	2005 Aug 8–10	i'	22 × 600	0.67
NGC 300 3	0 55 59	−37 50 59	2005 Oct 10–11, 31	g'	13 × 600	0.82
...	0 55 59	−37 50 53	2005 Sep 8, Oct 8–10	i'	22 × 600	0.72

Note. Units of right ascension are hours, minutes, and seconds, and units of declination are degrees, arcminutes, and arcseconds.

makes it well suited for stellar content studies. It lies at high galactic latitudes and therefore has low foreground reddening of $E(B - V) = 0.011\text{--}0.014$ mag (Schlegel et al. 1998), which translates into $E(g' - i') = 0.018\text{--}0.024$ mag. The high galactic latitude of Sculptor galaxies is also important because the contamination from the foreground Galactic stars is minimal at these high latitudes. In many respects NGC 300 is similar to the local spiral M33 (Blair & Long 1997). The optical disk scale length has been measured as 2.23 kpc in B_J (Carignan 1985) and 1.47 kpc in I (Kim et al. 2004). Tikhonov et al. (2005) and Butler et al. (2004) find that the stellar population is predominantly old and metal-poor, with no evidence for significant change in metallicity with time. The study of Puche et al. (1990) finds in NGC 300 an extended H I disk, which is severely warped in the outer parts ($10' < r < 20'$). The warp in H I disk has often been linked to the truncations in the stellar disk (van der Kruit 2007).

We adopt a distance modulus of 26.51 for NGC 300. This is a weighted-mean of distances determined from the Cepheid Variables (Freedman et al. 2001; Gieren et al. 2004) and the tip of the red giant branch (TRGB; Butler et al. 2004; Tikhonov et al. 2005).

The layout of the paper is as follows. We summarize the details of the observations and the data reduction in Section 2, and describe the photometric measurements and artificial stars test in Section 3. The color–magnitude diagrams (CMDs), star counts and surface brightness profiles, and the metallicity distribution function of NGC 300 are presented in Section 4. Finally, we discuss our results in Section 5.

2. OBSERVATIONS AND DATA REDUCTION

The deep g' and i' images of three fields in the outskirts of NGC 300 were obtained using the Gemini Multi Object Spectrograph (GMOS) on Gemini South telescope as a part of the program GS-2005B-Q-4; in total 34 hours of data have been taken. The observations are summarized in Table 1. The NGC 300 fields span a major axis distances of 7–16 kpc and were made to overlap slightly to allow for the check of the relative photometric calibration between the fields. The innermost field was placed at the optical edge identified in the Digitized Sky Survey (DSS) to provide continuity with the earlier work. The locations of the fields are marked in Figure 1. The field of view in a single GMOS image is $5'.5$ on a side; at the distance of NGC 300 $1'$ corresponds to 0.6 kpc.

The GMOS detector is a mosaic of three 2048×4608 EEV CCDs (Hook et al. 2004). The raw pixels were binned 2×2 during readout to provide a better match of the image sampling to the seeing, producing the pixels of $0''.146$ in size. The average image quality of the data is $0''.7$ FWHM in g' and $0''.6$ FWHM in i' .

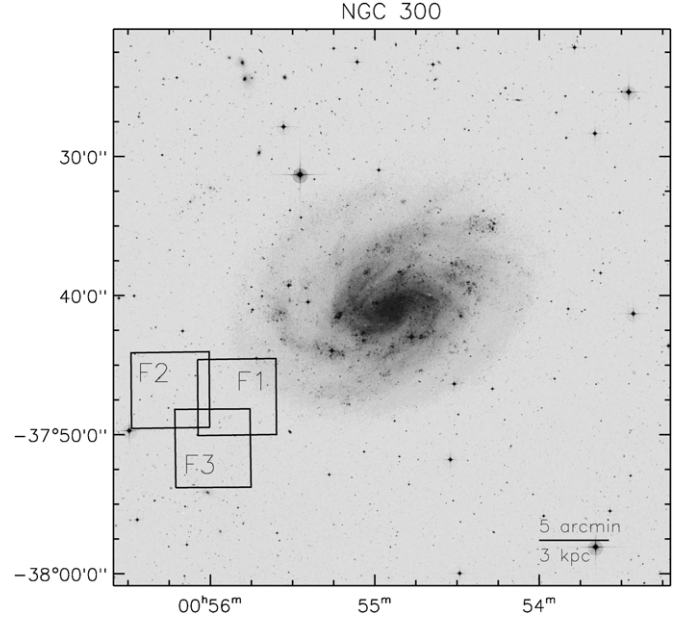


Figure 1. DSS wide-field image of NGC 300. (North is to the top, east is to the left.) Squares mark the positions of GMOS $5'.5 \times 5'.5$ field of view.

For each field, 13×600 s exposures were taken in g' and 22×600 s exposures in i' band. Our goal was to achieve 3σ photometry in g' and i' for a G giant star with ($V = 27.5$, $B = 28.5$, $I = 26.5$). The data were obtained in a dithered pattern, which allowed for the gaps between the individual GMOS CCDs to be filled when constructing the final image.

The data were reduced using the standard IRAF/Gemini routines. Due to the known problems with GMOS bias frames, we inspected all bias frames and discarded those in which the counts varied significantly between the subsequent frames. For the same reason, we decided to have the overscan regions subtracted in the reduction process. The processing pipeline included creating the master bias and flat field frames (gbias, giflat), bias subtraction and flat fielding (gireduce), mosaicking of individual GMOS CCDs into a single reference frame (gmosaic), and finally combining the dithered exposures into a final image (imcoadd). In addition, i' data were affected by fringing and the fringes needed to be removed. The master fringe frame was created for each field from the individual reduced image frames (gifringe) and subtracted from the individual images before coadding (girmfringe).

After the reduction procedure, the artifacts of mosaicking the GMOS CCDs into a single image were still present in g' data, visible as a background offset between the chips in the final images. The level of the offset was of the order of $\sim 1\%$ of the

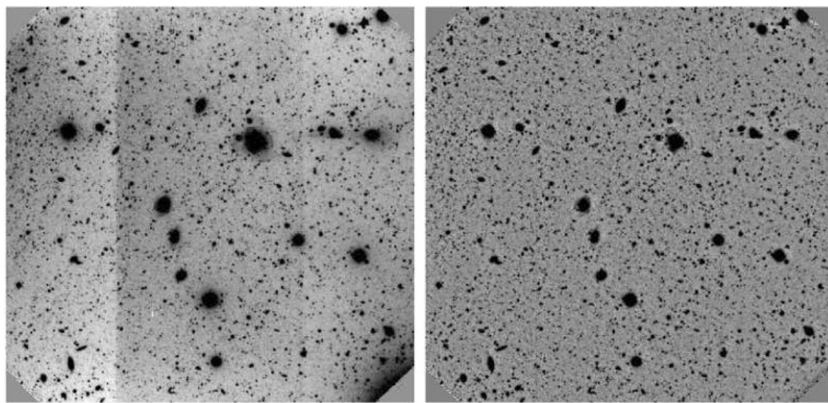


Figure 2. Reduced g' images of the NGC 300 F2 field. Left panel: the image after the standard reduction procedure has been applied (see the text for details). Right panel: the image after applying the additional fringe-removal procedure. This additional reduction step significantly improved the consistency of the background between the three GMOS CCD chips.

background, but was clearly evident upon visual inspection, as shown in the left panel of Figure 2. In order to attempt to remove these effects, we applied the same fringe-removal procedure on our g' data as described above for i' images. The procedure improved the background consistency between the chips; the example of the result for one of the fields is shown in the right panel of Figure 2.

3. PHOTOMETRY AND COMPLETENESS ANALYSIS

3.1. Photometry

The final g' - and i' -band GMOS images were analyzed using the DAOPHOT/ALLSTAR software suite (Stetson 1987). For each field DAOPHOT produced object catalogs and performed aperture photometry in a series of circular apertures. About 100–200 relatively bright and isolated stars in each field were chosen as PSF stars and used to iteratively compute the point-spread function (PSF) for the field. All PSF stars candidates were examined visually within the IRAF/DAOPHOT package and their radial, contour, and mesh profiles were inspected for any indications of their nonstellar nature. After the PSF stars were subtracted within the standalone DAOPHOT suite, the positions of subtracted PSF stars were inspected again using the above indicators. All PSF star which were not subtracted cleanly were excluded from the subsequent PSF calculations. In addition, stars which had PSF subtraction errors more than 3σ away from the mean value, as reported by standalone DAOPHOT package, were also excluded. The next iteration PSF was calculated from the image in which, within the fitting radius of each PSF star, all but PSF stars were subtracted. The procedure described above was repeated once more to derive the PSF; finally, ALLSTAR was used to fit this PSF to the objects in the catalogs and determine their PSF photometry.

In addition to the information on the object magnitude and the related error, ALLSTAR provides information on the quality of PSF fitting for each star through the parameters CHI and SHARP. CHI represents the ratio of the observed pixel-to-pixel scatter in the fitting residuals to the expected scatter. It is expected for the values of CHI to scatter around unity when plotted against the derived magnitude (e.g., Figure 28 of Stetson & Harris 1988). In our analysis, however, the values of CHI are scattered around ~ 0.4 . This may be indicative of the incorrect values for the gain and readout noise used in the analysis (P. Stetson 2008, private communication). The correspondence with Gemini staff confirmed that the gain and readout noise values used are indeed

correct and the reason for the invalid CHI values in ALLSTAR remained unclear. However, any photometric errors introduced by potentially incorrect gain and readout noise values will be taken into account through our artificial star tests which we use to estimate the observational uncertainties in the data.

The aperture corrections were calculated using the DAOGROW software (Stetson 1990), which performs a sophisticated growth-curve analysis to derive a “total” magnitude for each star. For each field, multiple-aperture photometry was done on the image frames from which all but PSF stars have been subtracted. The weighted mean difference between the PSF-based magnitude (from ALLSTAR) and the “total” magnitude (from DAOGROW) of the PSF stars was adopted as “aperture correction” and this correction was applied to PSF-based magnitudes of all stars in the frame. The uncertainties in the aperture correction over all bands and fields were 0.006–0.008 (the quoted uncertainty is the standard error of the mean).

The photometric calibration for the GMOS data was established using the Landolt (1992) standard star fields. The g' and i' magnitudes of standard stars were calculated using the relations from Fukugita et al. (1996). In total, six Landolt fields were observed multiple times over the two months run, with the total of ~ 140 standard stars observations. The total observed magnitudes of standard stars were measured using DAOGROW and the zero point was calculated as the difference between the observed magnitude corrected for the exposure time and the standard magnitude. Zero points varied by 0.02 between the standards stars observations on the different nights of the same month, or by 0.12 and 0.07 in g' and i' , respectively, over the two month period. Photometry was transformed onto a single calibration by comparing the magnitudes of stars in the overlapping regions, taking as a reference the field with the best calibration of the three (F1 in i' and F2 in g' , both observed during the 2005 August run). Results of the completeness analysis described below were used to confirm that the scatter of the photometry in the overlapping regions agrees with the scatter predicted from the artificial star tests.

3.2. Completeness Analysis

When interpreting stellar photometry of faint stars in crowded fields, it is important to understand the observational uncertainties inherent in the data. It is a standard procedure to use artificial star tests to estimate the completeness of the data and assess the effects the crowding has on the calculated magnitudes and their

errors. In the artificial star test a set of stars with known magnitudes is added to the frame, and the frame is analyzed using the standard data reduction pipeline to recover the photometry of all stars, real and artificial.

To be able to estimate the data completeness robustly, a large number of stars has to be added to the images and analyzed. This number should be significantly larger than the number of real stars detected in the image. At the same time, it is important not to affect the crowding of the images significantly, as that will result in the unrealistic estimates of completeness. As a compromise between the crowding in the field (where a small number of artificial stars is optimal) and the computing efficiency (where a large number of artificial stars is favorable as it decreases the total number of images that need to be analyzed), the number of stars that we add to each frame is 5%–10% of the number of detected stars in the frame. We then run a hundred tests on each image to obtain statistically robust estimate of the completeness and observational uncertainties.

In order to sample the crowding conditions in the frame correctly, artificial stars injected into the image must not overlap. To make certain that there is no overlap between the artificial stars, we add them to the frames in a regular grid. The grid has 30 stars on a side (i.e., 900 in total), with a separation of 69 pixels ($10''$) between neighboring stars. Our choice of the grid and cell size is guided by the considerations explained above and the need for the whole extent of the image to be sampled in each run. A total number of stars added to each frame over 100 artificial star test runs is $\sim 10,000$ per frame. The grid origin has been randomly offset between the runs in order to enable sampling of the whole extent of the image. The same grid setup is used to add artificial stars to one (g' , i') pair of images.

To assess the color effects, it is important that the colors assigned to artificial stars correspond to the realistic stellar populations. To ensure that the magnitude and color distribution of our artificial stars matches magnitudes and colors in the original data frames, we construct artificial photometry by randomly selecting stars from the original CMDs and assigning their g' and i' magnitudes to artificial stars.

Artificial stars with the positions and magnitudes determined as described above are added to the frames using the DAOPHOT/ADDSTAR routine. The resulting images are analyzed with the same data reduction pipeline as the original science frames, using the PSF calculated for each field as described above. A star is considered recovered if it is detected in both g' and i' frame and if the difference between the injected and recovered magnitude in both bands is < 0.5 mag. Completeness as a function of magnitude is calculated as the ratio of the number of recovered and injected stars in a given 0.5 mag bin. Completeness curves for three NGC 300 fields are shown in Figure 3. We compute the completeness in terms of the instrumental magnitude and then transform them using the appropriate photometric calibration equations into the completeness in terms of the standard magnitude. Our photometry is 50% complete down to (g' , i') = (26.8–27.4, 26.1–27.0).

To check the accuracy of the photometry, we calculate the difference between magnitudes of injected and recovered artificial stars. Figure 4 shows the difference between the input and output magnitudes as a function of the input magnitude for one of the observed fields. Over the most of the magnitude range in g' and i' the photometric error with which the stars are recovered is < 0.3 mag. There is a systematic trend over the whole magnitude range, with stars being recovered brighter than their true magnitude. Assuming that this effect is purely due to

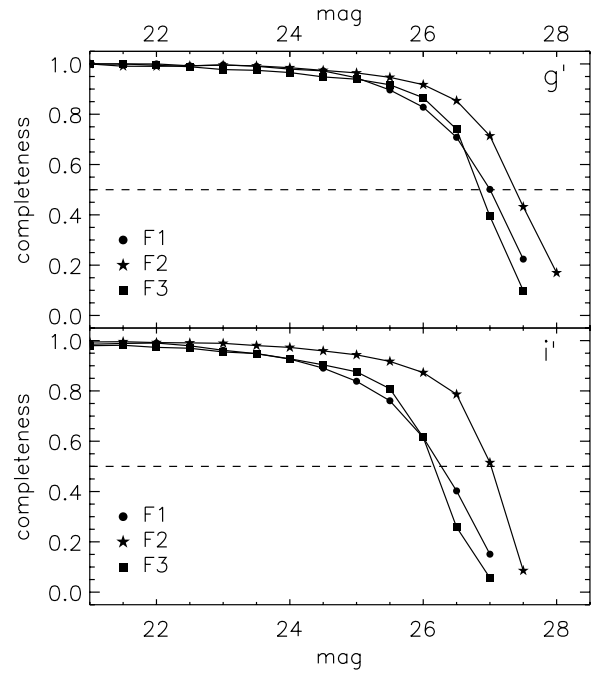


Figure 3. Completeness curves for the observed NGC 300 fields, in g' (top panel) and i' (bottom panel). The horizontal dashed line marks the 50% completeness limit.

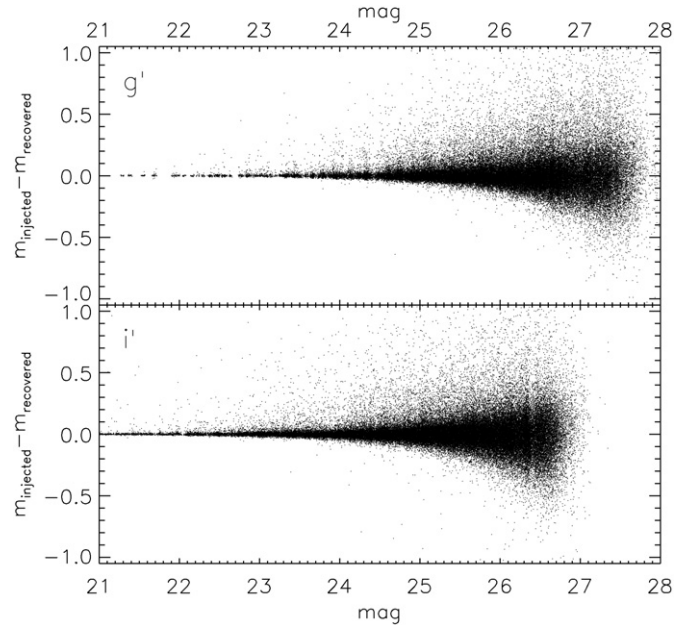


Figure 4. Difference between the injected and recovered magnitudes of all recovered artificial stars, in g' (top panel) and i' (bottom panel), for one of the observed NGC 300 fields. Only the stars with the difference between the input and output magnitude smaller than 0.5 were considered recovered when calculating completeness curves shown in Figure 3. Other NGC 300 fields show similar behavior.

blending, we estimate the blending fractions to be 5%–10% in F2 and F3 and $\sim 20\%$ in F1. However, the calculated blending fractions are an overestimate because at the faint end random fluctuations in the unresolved background may scatter faint stars below the detection limit, with only the stars lying on the positive background fluctuations being recovered.

We use artificial star tests to derive uncertainties of our photometry. We adopt as photometric errors the mean of the absolute value of the difference between the input and output

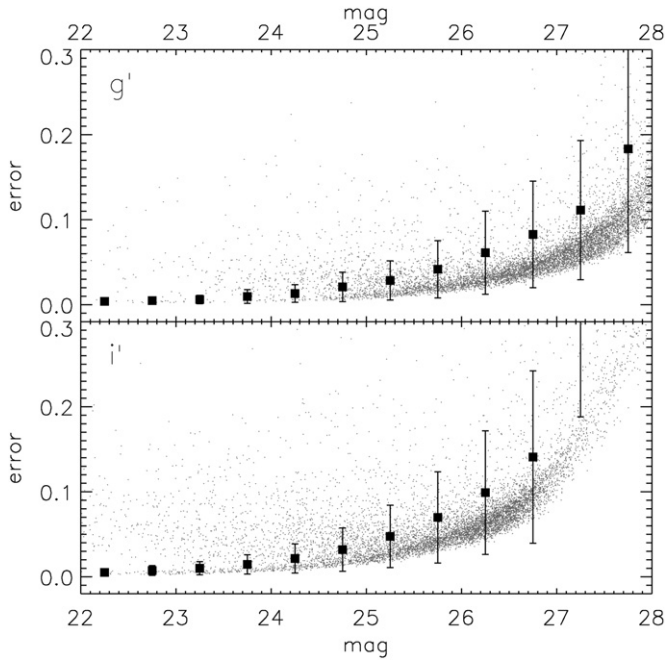


Figure 5. Photometric errors as given by ALLSTAR (gray points) and calculated from the artificial star tests (black squares); top panel shows the results for g' band, bottom panel for i' band data. Photometric uncertainties are derived from the artificial star tests as the mean difference between the input and output magnitudes of artificial stars in 0.5 mag bins. Error bars give the scatter in each bin.

magnitudes of artificial stars. Figure 5 shows the errors reported by ALLSTAR (points) and photometric uncertainties calculated from the artificial star tests as described above (squares), as a function of input magnitude. The error bars are the scatter in each 0.5 mag bin. At the faint end the errors derived from the artificial star tests are ~ 0.04 mag larger than the errors given by ALLSTAR.

In addition to estimating completeness and photometric errors, we use the artificial stars tests to discard the nonstellar and spurious detections. Due to the nonstandard CHI output of the ALLSTAR routine (see Section 3.1), we are not able to apply commonly used cuts in CHI parameter to reject false detections. With the artificial star tests however, we are able to use the information on CHI and SHARP of the artificial stars to set the criteria for removing the false detections from the data. In Figure 6, we show the distribution of CHI and SHARP parameters for the real stars (black points) and all recovered artificial stars (gray points) as a function of magnitude, for one of the observed NGC 300 fields. In order to remove nonstellar objects from the sample, we employ cutoffs based on the values of SHARP parameter of the recovered artificial stars. We divide the data into 0.5 mag wide bins and discard objects that are more than 3σ away from the mean value of SHARP in a given bin. The dashed curve in the top panel of Figure 6 shows the extent of the allowed SHARP values. In addition, we use a constant CHI limit and remove from the stellar catalogs all stars with $\text{CHI} > 0.5$.

4. RESULTS

4.1. Color–Magnitude Diagram

We show the $(g' - i', i')$ CMDs of the three observed NGC 300 fields in Figure 7. The most prominent component of these CMDs is the well populated RGB. This feature is typical of a system composed of a stellar population older than 1 Gyr. In

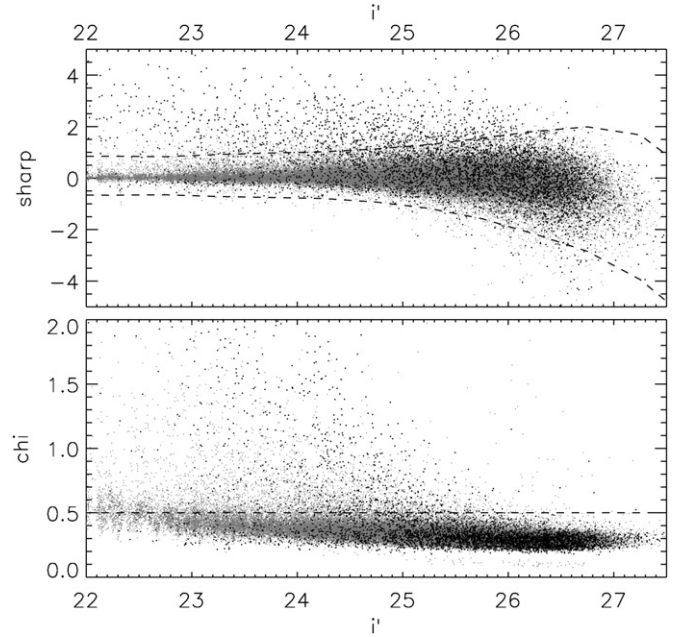


Figure 6. Values of the CHI (bottom panel) and SHARP (top panel) parameters as reported by ALLSTAR for all recovered artificial stars (gray) and the real stars (black). Dashed lines are the cuts in CHI and SHARP used to discard spurious detections.

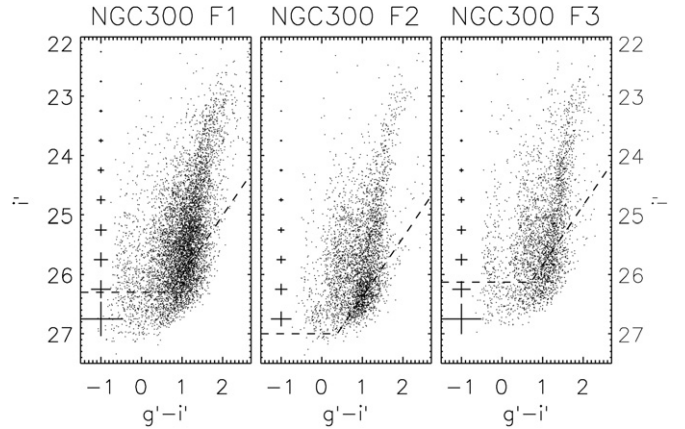


Figure 7. CMDs of the three NGC 300 fields. Error bars show the photometric uncertainties from the artificial star tests at a given i' magnitude and the color of $g' - i' = 1$. The dashed lines indicate the 50% completeness limit.

all observed fields the red giants branch stars make up $\sim 50\%$ of all stars detected in the field. A small number of red stars is found above the tips of the theoretical RGB tracks (Figure 8); these stars could be intermediate-age asymptotic giant branch stars and young red supergiants. Also marked on the CMDs in Figure 7 are the 50% completeness limit and the photometric errors at a given i' magnitude and $g' - i'$ color of 1, as determined from the artificial stars tests (Section 3.2).

In addition to the dominant old and red stellar population, we detect a sparsely populated MS with $g' - i'$ colors from -1 to ~ 0 . This feature contains 10% of the stars detected in the outer disk of NGC 300 and most likely represents MS stars with the ages of a few hundred Myr.

4.2. Star Counts Profile

In our previous study of the outer regions of NGC 300 (Bland-Hawthorn et al. 2005), we used r' star counts to trace the faint stellar disk out to 15 kpc ($25'$). Now with the multiband

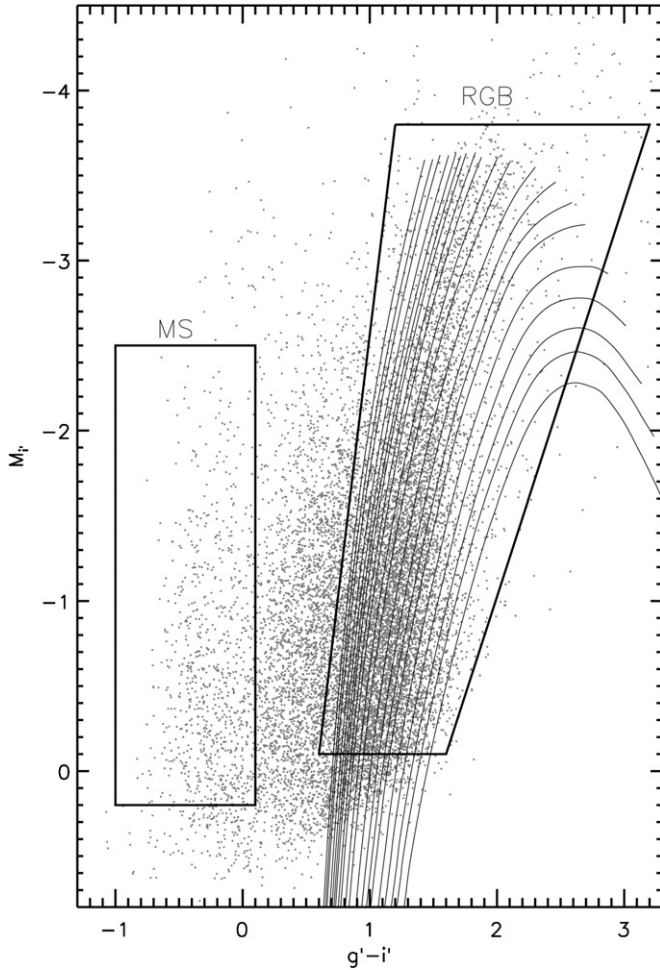


Figure 8. CMD of the three NGC 300 fields, with the Victoria–Regina (VandenBerg et al. 2006) set of $[\alpha/\text{Fe}] = 0.0$, 8 Gyr stellar evolutionary tracks overplotted. The model grid has the metallicities in the range $[\text{Fe}/\text{H}] = [-2.31, 0.00]$. Two regions marked in the figure were used to select stars belonging to RGB and MS population.

photometry in hand, we can refine our radial profile to target distinct stellar populations in the outer disk of NGC 300.

We derive the radial profile of the RGB and MS stars by counting the stars in elliptic annuli with the ellipticity (inclination) and position angle corresponding to that of NGC 300 ($\text{PA} = 110^\circ$, $i = 42^\circ$). In Figure 8, we reproduce the CMD of the NGC 300 F1 field and define the selection boxes we use to select RGB and MS stars. To account for the crowding effects we compute completeness as a function of galactocentric distance using the output of the artificial stars tests described in Section 3.2. This is calculated as a ratio of the number of recovered to injected stars in each 0.5 radial bin and used to correct star count profiles. The resulting completeness-corrected profiles of RGB and MS stars are shown in the top panels of Figure 9.

In order to be able to derive the intrinsic star counts profile, it is crucial to as reliably as possible estimate the contribution of the contaminant sources—dwarf stars in the Galaxy and faint unresolved background galaxies that get mistaken for NGC 300 stars. Given the high galactic latitude of NGC 300 ($b = -79.4$) we do not expect the contribution from galactic dwarfs to be significant. Besancon models (Robin et al. 2003) predict 26 stars per GMOS field of view in the magnitude and color range corresponding to our RGB selection box; this accounts for 0.5%–1% of all detected objects in a single field with the same color–magnitude criteria.

The online GALAXYCOUNT calculator (Ellis & Bland-Hawthorn 2007) is a useful tool for estimating galaxy counts in deep wide-field images. It had confirmed our earlier finding that even when the contribution from the faint unresolved galaxies is accounted for, the exponential disk of NGC 300 as traced by r' -band star counts extends out to 10 disk scale lengths (Bland-Hawthorn et al. 2005; Ellis & Bland-Hawthorn 2007). However, we now derive star count profiles for different stellar populations which populate distinctive regions in the color–magnitude space (Figure 8) and require information on the color, as well as magnitude, of the background galaxy population. Since GALAXYCOUNT at present does not include the

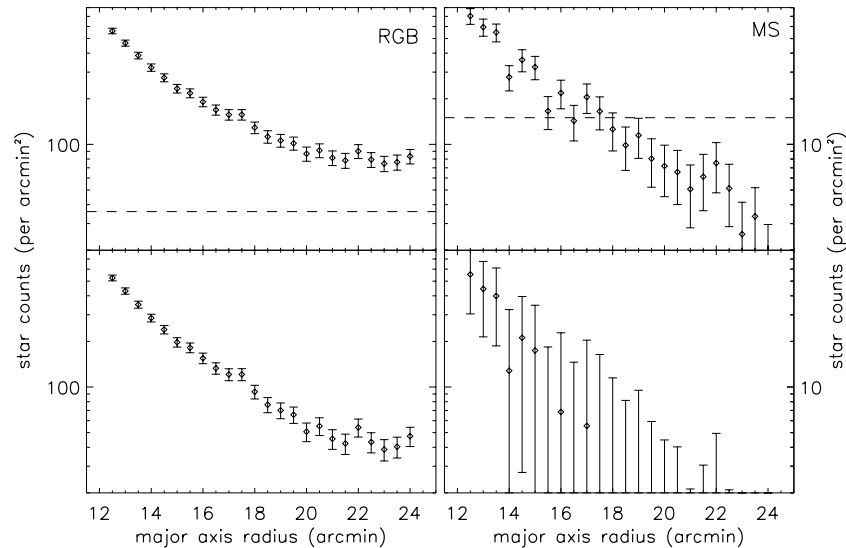


Figure 9. Star counts profile of the RGB (left panels) and MS stars (right panels) in the outer disk of NGC 300. Stars inside the regions marked in Figure 8 were used to calculate the profile. The top panels show the profiles before the contribution of the faint unresolved galaxies has been subtracted. The dashed line corresponds to the predicted number of background galaxies (arcmin^{-2}) with the colors and magnitudes within our RGB and MS selection boxes. The bottom panels show the star count profiles corrected for the background galaxies contribution.

color information, we can only estimate the number counts predicted in g' and i' bands separately. For example, in the case of our RGB selection box (Figure 8) GALAXYCOUNT predicts 82–114 galaxies in the magnitude range $g' = 23.9$ –28.0 and 114–140 galaxies in the range $i' = 22.7$ –26.4. To estimate the galaxy number counts, we use the completeness curves derived separately for each field; the range in the number counts estimates reflects the differences in the parameters describing the completeness curves for different fields. However, the number counts predicted by GALAXYCOUNT are an overestimate of the true contamination within our RGB selection region because (1) they are derived without any restrictions on the color of the background galaxy population and (2) a number of contaminating galaxies have already been somewhat reduced by the use of the SHARP statistic.

For the reasons described above, we chose to use the galaxy counts from the William Herschel Deep Field (WHDF; Metcalfe et al. 2001) to estimate the contamination from the faint background galaxy population. The main caveat with this kind of approach is that the WHDF survey is not as deep as our data and some assumptions need to be made in order to estimate the number counts of galaxies in our data using a shallower survey. We calculate the i' -band number counts of the galaxies falling within our color selection criteria and fit linearly the (log of) differential number counts in 0.5 mag bins in the range covering 3 mag above the WHDF magnitude limit. To determine the galaxy counts below the limit of the WHDF survey, we assume that the counts in the bins 2–3 mag below the survey limit follow the same linear trend (in the log space) as the counts in the brighter bins used in the fit. We finally take into account the incompleteness of our own data and correct the derived galaxy number counts using the completeness curves presented in Figure 3. The estimated mean number of unresolved background galaxies over all fields is $36 \pm 7 \text{ arcmin}^{-2}$ for our RGB selection box and $15 \pm 8 \text{ arcmin}^{-2}$ for the region used to select the MS stars. The errors represent a combination of the variation of the estimated galaxy counts between the three fields and the cosmic variance. The latter was estimated using GALAXYCOUNT, which for given galaxy number counts in a given magnitude range calculates the expected variance. The star count profiles before and after subtraction of the background galaxy population are shown in Figure 9, in top and bottom panels, respectively. Error bars in the bottom panel are a combination of errors quoted above and Poisson uncertainties. Under the assumption that the slope of the WHDF number counts changes at the survey magnitude limit to a value twice that derived from the bins 3 mag below the survey limit, we derive the galaxy counts as 80 ± 15 and $29 \pm 14 \text{ arcmin}^{-2}$ for our RGB and MS selection, respectively. After the subtraction of the newly determined galaxy counts, the old stellar disk remains purely exponential but falls below the detection limit at $\sim 20 \text{ arcmin}$. However, these higher counts are very likely to be an unrealistically high estimate for the contribution from the background galaxy population, given that they are significantly higher than our MS star counts in the outermost two thirds of our MS radial profile.

As Figure 9 clearly shows, while the old stellar disk extends out to $25'$, corresponding to 15 kpc, the young MS stellar population is more centrally concentrated and is only detected out to $17'$ (10 kpc) along the southern end of the major axis. The disk, as traced by the old stellar population, does not exhibit a break in surface brightness profile once the star counts have been corrected for the contamination by unresolved

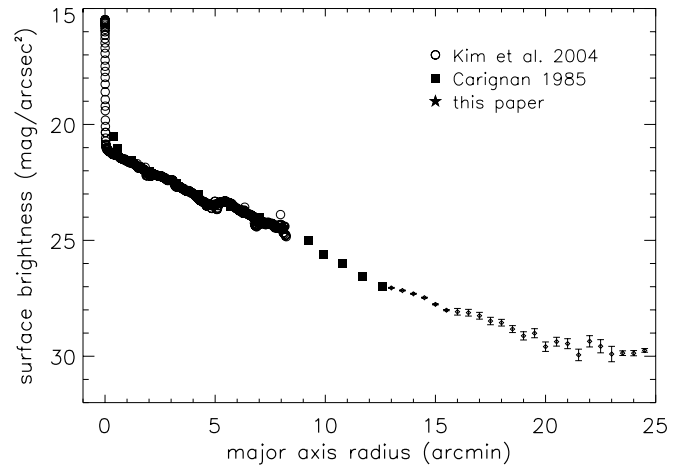


Figure 10. Surface brightness profile of NGC 300. Open circles are i -band surface photometry data from Kim et al. (2004); the data points have been shifted downward by 1.2 mag. Full squares are B_J surface photometry measurements taken from Carignan (1985) and have been shifted upward by 0.4 mag. The star symbols are our surface brightness measurements derived from star counts.

background galaxies. This complements our finding of an unbroken exponential disk in late-type galaxy NGC 300 out to the distances corresponding to about 10 disk scale lengths (Bland-Hawthorn et al. 2005).

4.3. Surface Brightness Profile

In Figure 10, we derive the surface brightness profile of the outer disk of NGC 300 from the i' -band starcounts of the old RGB stars. The inner data points in this figure are taken from the surface photometry studies by Kim et al. (2004) and Carignan (1985). The outer disk surface brightness is calculated in 0.5 annuli by summing the flux of all stars in a given annulus and correcting for the radial completeness, number of pixels in the annulus and the pixel scale to obtain surface brightness in the units of mag arcsec^{-2} . We correct for the background galaxy contamination by randomly removing from each radial bin a number of objects corresponding to our estimate of the galaxy number counts (36 arcmin^{-2}) corrected for the area of the annuli. We repeat this process by drawing 100 random “background galaxy-corrected” samples from our full stellar catalog and use this to calculate the final value of surface brightness in each radial bin, and estimate its error bars (as standard deviations of the full set of 100 samples). Finally, we correct for the light missed due to the fact that we detect only the brightest stars in the outskirts of NGC 300 and the inclination of the galaxy. In Bland-Hawthorn et al. (2005), we estimate the fraction of missing light to be $\sim 45\%$ for a study of a similar photometric depth. This translates to intrinsic surface brightness 0.65 mag brighter than what we derive here. The galaxy inclination ($i = 42^\circ$) somewhat counteracts this effect; if the galaxy was viewed face-on, the resulting surface brightness would be 0.32 mag fainter. Therefore, to account for both effects, the calculated surface brightness has to be shifted upward by 0.33 mag.

The surface brightness profile in Figure 10 emphasizes the power of resolved star counts over the traditional diffuse light imaging for reaching down to very low surface brightness levels necessary for studying the extremely faint outskirts of galaxy disks.

4.4. Metallicity Distribution Function

Given the CMD and the distance to NGC 300, we are able to compute the metallicity distribution function of the stellar populations in its outskirts. Theoretical isochrones show that metallicity (rather than age) is the primary factor affecting the color of the RGB (VandenBerg et al. 2006; see also Figures 5 and 6 of Harris et al. 1999); for example, at absolute magnitude $M_I = -3$ the 0.2 mag blueward shift in $V - I$ can be achieved by a decrease in age from 13 to 6 Gyr, or by a relatively small decrease in $[\text{Fe}/\text{H}]$ from -1.0 to -1.2 (Mouhcine et al. 2005). This high sensitivity of photometric properties on metallicity allows us to derive the metallicity distribution function from the photometry of the RGB stars.

To derive the metallicity distribution function, we convert the observed distance- and reddening-corrected stellar photometry to metallicity on a star-by-star basis. We superimpose on observed CMD the stellar evolutionary tracks of VandenBerg et al. (2006) and interpolate between them to derive an estimate of star's metallicity (Figure 8). The model grid consist of 16 finely spaced red giant tracks for an 8 Gyr stellar population without α -enhancement, covering the range of metallicities from $[\text{Fe}/\text{H}] = -2.31$ to 0.00 in the steps of approximately 0.1 dex. We define a region in $(g' - i', i')$ which we expect to be populated primarily by RGB stars and only consider the stars within this selection box when calculating metallicities (Figure 8).

In computing the metallicity distribution function, we choose to use the theoretical stellar evolutionary tracks rather than empirical globular cluster fiducials. The grid of RGB tracks from VandenBerg et al. (2006) on which we base our metallicity estimates is much more finely spaced than often used Milky Way globular cluster fiducials by Saviane et al. (2000); as shown by Harris et al. (1999) and Harris & Harris (2000), the coarseness of the model grid may introduce artifacts in the calculated metallicity distribution function. By inspection of Figure 8, it is clear that the stars in the outer regions of NGC 300 are metal-poor and there is no need for adding stellar tracks more metal-rich than those present in the VandenBerg et al. (2006) grid.

In order to take into account the incompleteness effects we compute the completeness-corrected metallicity distribution function by counting each star $(C_{g'}C_{i'})^{-1}$ times, where $C_{g'}$ and $C_{i'}$ are completeness in g' and i' at a given point in the CMD. We only consider stars which fall above 50% completeness limit in both g' and i' . For fainter stars, the completeness correction factor becomes too large and not necessarily a realistic representation of the incompleteness effects which are poorly understood at these faint magnitudes.

The presence of stars of different ages will affect our metallicity estimates which utilize the 8 Gyr stellar tracks; the effect is illustrated in Figure 11. The solid line is the metallicity distribution function calculated using the stellar tracks for the 8 Gyr stars with no α -enhancement. Also shown are the metallicity distributions constructed assuming an older age (12 Gyr, dashed line) and different value for α -enhancement ($[\alpha/\text{Fe}] = 0.3$, dotted line). If the true stellar population is older or more α -enhanced than our adopted stellar evolutionary tracks, this procedure will have overestimated the number of high-metallicity stars, and similarly, underestimated the contribution of low-metallicity stars, but the effect on the peak metallicity of the stellar population will not be significant.

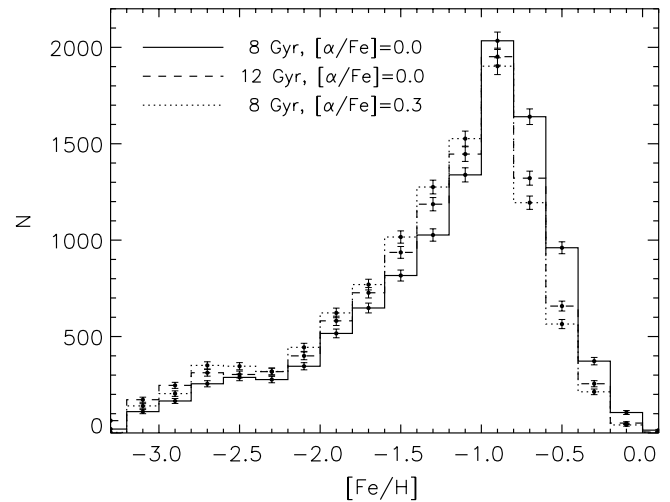


Figure 11. Metallicity distribution function of NGC 300 stars calculated using the Victoria–Regina stellar evolutionary tracks with the age of 8 Gyr and no α -enhancement. Also shown are the metallicity distribution functions calculated assuming the stellar ages of 12 Gyr and $[\alpha/\text{Fe}] = 0.0$ (dashed line) and an 8 Gyr old stellar population with $[\alpha/\text{Fe}] = 0.3$ (dotted line). If the stellar population in the outskirts of NGC 300 is α -enhanced or older than the assumed age of 8 Gyr, our procedure will have slightly overestimated the number of stars at the high-metallicity end, but without a significant effect on the mean metallicity of the population.

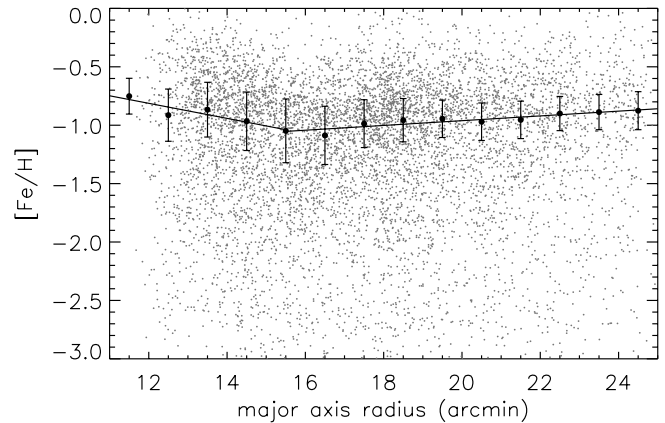


Figure 12. Metallicity as a function of radius for all stars in the outer disk of NGC 300. Full circles are the median metallicities in $1'$ bins. Solid lines represent the metallicity gradient and are a linear fit to the median metallicities in the range $R < 15.5$ and $R > 15.5$. Error bars represent the mean uncertainty in $[\text{Fe}/\text{H}]$ in each bin.

4.4.1. Metallicity Gradient

In Figure 12, we plot metallicity as a function of deprojected galactocentric radius for all stars in the outer disk of NGC 300. Preliminary analysis of stellar metallicities has shown that metallicity decreases with radius out to about 15.5 after which the gradient becomes mildly positive. We therefore divide the data into $R < 15.5$ and $R > 15.5$ (9.3 kpc) bins and independently calculate the metallicity gradient (in dex kpc^{-1}) for each region, by fitting linear functions to median metallicities in $1'$ wide radial bins:

$$R < 15.5 : [\text{Fe}/\text{H}] = -0.11(\pm 0.02)R - 0.04(\pm 0.15),$$

$$R > 15.5 : [\text{Fe}/\text{H}] = 0.034(\pm 0.004)R - 1.37(\pm 0.06).$$

Despite the large scatter in calculated metallicities, we clearly detect both the negative abundance gradient out to ~ 9.3 kpc and a change in the trend outward of 9.3 kpc.

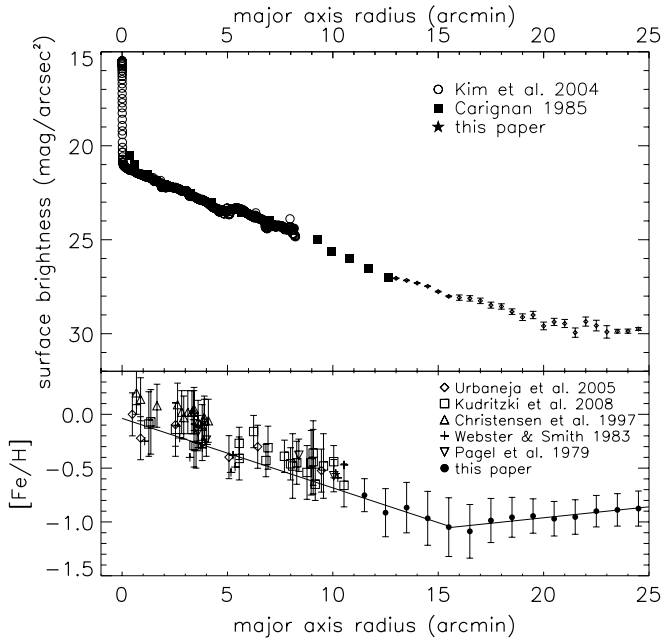


Figure 13. Top: surface brightness profile of NGC 300. Bottom: metallicity gradient in the disk of NGC 300. Inner disk data points are from the spectroscopic abundance studies listed in the figure. Filled circles are outer disk binned mean metallicities and solid lines are the linear fits to these values as calculated in Figure 12.

Figure 13 shows the pure exponential surface brightness profile of NGC 300 and its metallicity gradient on the same radial scale. In the bottom panel of this figure, we compile the available data on the inner disk metallicities from the literature. All metallicities except the recent Kudritzki et al. (2008) results refer to oxygen metallicities only, and all except Kudritzki et al. (2008) and Urbaneja et al. (2005) metallicities are derived using the H II region emission lines.

The reasons for the metallicities we derive being seemingly too low compared to the spectroscopic metallicities in the central regions of NGC 300 are twofold. First, the inner disk metallicities in Figure 13 either represent gas, rather than stellar, metallicities, or were measured from young blue supergiants, both of which are expected to have higher metallicities than the older RGB stars at the same radii. Second, as can be seen from Figure 12, the bulk of the stars populate the high-metallicity end of the plot and it is the low-metallicity tail of the abundance distribution function (see Figure 11) that is responsible for lower mean metallicities. Since we base our discussion primarily on the overall shape of the metallicity gradient, rather than the absolute value of metallicities this effect will not influence our conclusions.

In order to test the robustness of the derived abundance gradient, we performed a series of tests in which we randomly removed from the sample (1) a constant number of stars, corrected for the different areas of elliptic annuli, or (2) a number of stars proportional to the number density of stars in a given radial annuli. These procedures mimic the effect of correcting for the (1) constant contamination (e.g., background galaxies, stellar halo) and (2) radially dependent contamination (e.g., thick disk). Only after artificially removing 50% of stars in each bin are we able to derive a flat abundance gradient over the full radial extent sampled by our data. However, there is no realistic mechanism that could account for a 50% contamination level within our RGB selection region and hence we consider our derived abundance gradient to be robust.

5. DISCUSSION

In this paper, we revisit NGC 300 to investigate the faint stellar population in its outer disk. We confirm the earlier finding (Bland-Hawthorn et al. 2005) of the extended stellar disk in NGC 300 with the surface brightness declining exponentially out to $\sim 25'$, or about 10 disk scale lengths (Section 4.2). Only three other disks so far have been traced down in resolved stars to the same effective surface brightness levels—that of the Galaxy (Ibata et al. 2003), M31 (Irwin et al. 2005), and M33 (Ferguson et al. 2007). Except for the case of a “sub-exponential” disk of M33, the other three disks are either pure exponentials or “superexponential” and are detected down to the effective surface brightness levels below ~ 30 mag arcsec $^{-2}$. The existence of stars at these extremely low surface densities in the outer galactic disks is puzzling. We want to learn what the nature of the faint stellar population in NGC 300 is and whether its outer disk is young or old. The answers to these questions will have important implications for the scenarios for the formation of spiral galaxies. With the multiband imaging in hand, we are now able to assess the ages and metallicities of stars in the outskirts of this late-type spiral.

From the $(g' - i', i')$ CMDs of NGC 300 presented in Section 4.1 and the star count profiles of RGB and MS stars (Figure 9), we find that its outer disk is predominantly old. Old outer disks are in disagreement with the inside-out picture of spiral galaxy formation in which the inner disk is built up on shorter timescales than the outer disk and young stars are expected to inhabit the larger radii (Larson 1976; Matteucci & Francois 1989; Chiappini et al. 1997; Naab & Ostriker 2006). This is however not the first time the old stellar population has been discovered at large galactocentric distances. Ferguson & Johnson (2001) use the Wide Field Planetary Camera 2 on board *Hubble Space Telescope* (HST) to observe a field on the major axis of M31 at the radius corresponding to three disk scale lengths. Using the mean *I*-band magnitude of the red clump as an age indicator, they find that the mean age of the stellar population in the outskirts of M31 is > 8 Gyr. In their studies of the outermost regions of M33, Galletti et al. (2004) and Barker et al. (2007) both find that the young MS stars appear to be more centrally concentrated and hence have smaller scale lengths than the older RGB population. The disks that have formed inside-out however have stellar populations which get progressively younger with radius and the oldest disk stars have the smallest scale lengths, in contrast to what is observed in M33 (Matteucci & Francois 1989; Chiappini et al. 1997; Galletti et al. 2004; Barker et al. 2007).

It may be possible to reconcile the two results in the context of models by Roškar et al. (2008a). In their simulations of spiral galaxy formation, the old outer disks arise as a consequence of stellar migrations from the inner disk. Star formation rate density falls off sharply at the radius of a break in the radial profile, but the stars are found in the outer disk at least ~ 5 kpc beyond the break. They find that about 85% of these stars have formed in the inner disk and subsequently migrated outward, beyond the truncation radius. The break in the surface density coincides with the minimum mean stellar age in the disk. Inward of the break younger stars populate the larger radii, but the trend is reversed once we cross the point of truncation. In this scenario, the outermost regions of disks are old because the old stars have had the most time to migrate farthest out in the disk. While the positive age gradient in Roškar et al. (2008a) models could succeed in explaining the Galletti et al. (2004) and Barker et al. (2007) results for the outer disk of M33, it is not clear whether

the same mechanism would produce the old outer disk in the purely exponential disk of NGC 300.

The question that arises here is whether what we observe as an extended stellar disk is in fact a halo component in NGC 300. Tikhonov et al. (2005) use *HST*/ACS to study the outer disk of NGC 300 and attribute the red giants found in their outermost field at $13'$ to a halo population. However, our surface brightness profile of NGC 300 in Figure 10 confirms that the outer disk indeed follows the same exponential profile as the inner disk and hence is not a distinct population. The possible reasons for a discrepant result reported by Tikhonov et al. (2005) are twofold. Their outer field spans only $2'$ with large variations of star counts within the field, and they do not account for the contribution to the star counts by faint background galaxies. Correcting for the contamination from the unresolved galaxy population would have the effect of steepening the profile in the outer field and making its slope more similar to the slope derived from their innermost fields.

Using the color of the stars on the RGB as a proxy for their metallicity, we derive the metallicity distribution function of the stars in the outskirts of NGC 300 and find that metallicity gradient changes slope at a radius of $15.5' (\sim 9.3 \text{ kpc})$. Does this mark the end of the disk in NGC 300 and a transition to an old halo? The argument against halo domination at large galactocentric radii is the relatively high metallicity in the outermost $10'$. Typical stellar halos are more metal-poor than what we find for the outer disk of NGC 300. In the Local Group, the halos of the Galaxy (Beers et al. 2005; Carollo et al. 2007; Ivezić et al. 2008) and M31 (Chapman et al. 2006; Koch et al. 2007) have metallicities of the order of $[\text{Fe}/\text{H}] = -1.5$, or lower. Even the less massive, almost bulge-less M33, believed to be a local analog of NGC 300, has a metal-poor halo with $[\text{Fe}/\text{H}] = -1.3$ to -1.5 (Brooks et al. 2004; McConnachie et al. 2006), and a more metal-rich disk with the photometric metallicity of $[\text{Fe}/\text{H}] \approx -0.9$ (McConnachie et al. 2006), similar to the outer disk metallicities we derive. We also note here that stellar halos are usually found to exhibit a negative metallicity gradient (Harris 1996; Parmentier et al. 2000; Koch et al. 2007), which is in disagreement with our positive or flat gradient in the outer disk. However, due to the limited radial extent of our data, this is not as strong of an argument against the halo domination at large radii as are the high metallicities found in our outermost field.

Negative abundance gradients are a common feature of disk galaxies. The dependence of yield, star formation, and gas infall on the galactocentric radius in chemical evolution models reproduces the gradients (Goetz & Koeppen 1992; Matteucci & Francois 1989), which are shallow and with a large but uniform dispersion. A metallicity trend in which the decline in abundances with radius is followed by a metallicity plateau, and which we find in the outer disk of NGC 300, may be a general property of spiral disks. It has so far been observed in all of the galaxies for which the deep stellar photometry is available—M31, M33, and the Galaxy. Worthey et al. (2005) use archival *HST* images of a number of fields spanning the galactocentric distances out to 50 kpc to derive abundance gradient in the disk of M31. While the inner disk exhibits a negative metallicity gradient, as expected from the chemical evolution models, the gradient disappears at $\sim 25 \text{ kpc}$ with the metallicity remaining nearly constant in the outer disk at $[\text{M}/\text{H}] \approx -0.5$. Yong et al. (2005, 2006), and Carney et al. (2005) find a similar metallicity plateau at the radius of 10–12 kpc in the outer disk of the Galaxy. They also observe the α -enhanced outer disk with $[\alpha/\text{Fe}] \approx 0.2$.

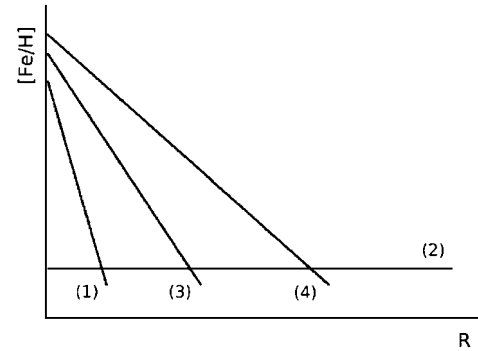


Figure 14. Illustration of a working model for the evolution of abundance gradients in disks. (1) Central spheroid is formed at high redshift and intense star formation establishes the steep metallicity gradient. (2) The metal-poor and uniform-metallicity disk is assembled at $z \sim 2$. (3) Star formation migrates to progressively larger radii and enriches the initially low-metallicity regions. (4) As a consequence, the abundance gradient continues to flatten.

Similar results are those of Twarog et al. (1997) who find the break in the metallicity gradient of open clusters at $R \approx 10 \text{ kpc}$, with the constant metallicity at larger galactocentric distances. In their deep ACS study of the M33 outer disk, Barker et al. (2007) see an indication for the flattening in the metallicity gradient beyond the radius of $50'$. The same effect has also been recently detected through the oxygen abundances of H II regions in M83 (Bresolin et al. 2009).

We present here two scenarios to explain the metallicity plateau (or upturn) in the outer disks of spirals.

In the radial mixing scenario, the mechanism described by Sellwood & Binney (2002) is responsible for transporting the stars within the disk while preserving the nearly circular orbits and exponential light profile. In Bland-Hawthorn et al. (2005), we show that the outer disk of NGC 300 is a high- Q environment (with the Toomre Q parameter of $\sim 5 \pm 2$) and as such is expected not to be responsive to gravitational disturbances, such as star formation or spiral waves. If however there is a mechanism that could lower the estimated value of Q (e.g., presence of cold gas that is unaccounted for in our earlier calculation of Q which estimates the surface density from the H I observations), scattering of stars by spiral waves (Sellwood & Preto 2002) could possibly explain the existence of stars in these diffuse regions. Potentially, stellar migrations could also explain the flattening or upturn we observe in the metallicity gradient of NGC 300. Models of Roškar et al. (2008b) reproduce the negative abundance gradient in both interstellar medium (ISM) and stars but show that the two abundance tracers evolve in opposite manner once the assumption of stars remaining in-situ is relaxed. Stellar radial mixing has had a stronger cumulative effect on older stellar populations, causing the stellar abundance gradient to appear flatter at early times, contrary to abundance gradient in the ISM. In their model, the same mechanism is responsible for the observed flattening of the intermediate-to-old population stellar abundance gradient in the outermost disk, similar to what we observe in the outer regions of NGC-300. However, scattering over such large distances (5–8 kpc) might require spiral waves much stronger than those considered by Sellwood & Binney (2002). We note that in addition to scattering by transient spiral arms, stellar migrations could also be caused by a passing perturber, as discussed by Quillen et al. (2009).

The accretion scenario is illustrated in Figure 14. In this picture, the central spheroid is assembled first in the early universe ($z > 4$). The first generations of stars that form

establish a steep abundance gradient in the spheroid (1), reaching the metallicities of around solar. This is supported by solar metallicities seen in QSOs at high redshifts (Hamann & Ferland 1999, and references therein) and steep abundance gradient in the old stellar bulge of the Galaxy (Zoccali et al. 2008; Feltzing & Gilmore 2000; Frogel et al. 1999; Minniti et al. 1995; but see Ramírez et al. 2000; Rich et al. 2007). The disk component is established at $z \sim 2$ (Wolfe et al. 2005). The initial disk is metal-poor and with uniform abundance (2), reflecting the metallicities in the intergalactic medium (IGM) at the formation redshift. As the galaxy is built in the inside-out fashion, the extent of star formation migrates toward the outer disk and the parts of the disk that previously had pristine abundances are now forming metals (3). This is a consequence of the gas and stellar density building up in the outer disk. As a result, regions of the disk at progressively larger radii become enriched and abundance gradient flattens with time (4). Observations of a variety of chemical gradients in PNe (Maciel et al. 2003, 2006), open clusters (Friel et al. 2002; Chen et al. 2003), cepheids, OB associations (Maciel et al. 2005; Daflon & Cunha 2004) and H II regions (Maciel et al. 2007) have shown that older objects exhibit steeper abundance gradients resulting in chemical gradients that become flatter with time. We note however that while some of the chemical evolution models that incorporate inside-out growth of galactic disks are able to reproduce this behavior (Molla et al. 1997; Boissier & Prantzos 1999; Portinari & Chiosi 1999; Hou et al. 2000), others predict steepening of gradient with time (Tosi 1988; Chiappini et al. 2001). This demonstrates the sensitivity of abundance gradients on adopted form of the radial dependence for the star formation and gas infall.

A simple consequence of this picture is that there exists a radius in a galactic disk at which a transition occurs between the star-forming disk with a negative abundance gradient and a uniform-abundance initial disk, as observed here in the case of NGC 300, as well as in the disks of the Galaxy (Yong et al. 2005, 2006; Carney et al. 2005) and M31 (Worthey et al. 2005). The outer disk abundances reflect the local metallicity floor, which is supported by enhanced $[\alpha/\text{Fe}]$ ratios and low $[\text{Fe}/\text{H}]$ both in external gas locally (Collins et al. 2003, 2007) and in the IGM at high redshift (Prochaska et al. 2003; Dessauges-Zavadsky et al. 2004, 2006).

The accretion scenario suggests that stars today were born roughly in situ, whereas the radial mixing scenario implies that stars largely migrate away from where they were formed. Both of these have consequences for future studies of disk formation.

We thank the anonymous referee for helpful comments, James Binney for useful discussion, and Peter Stetson for providing his DAOPHOT package. Based on observations obtained at the Gemini Observatory, which is operated by the Association of Universities for Research in Astronomy, Inc., under a cooperative agreement with the NSF on behalf of the Gemini partnership: the National Science Foundation (United States), the Science and Technology Facilities Council (United Kingdom), the National Research Council (Canada), CONICYT (Chile), the Australian Research Council (Australia), Ministério da Ciência e Tecnologia (Brazil), and Ministerio de Ciencia, Tecnología e Innovación Productiva (Argentina).

Facilities: Gemini (GMOS).

REFERENCES

- Bakos, J., Trujillo, I., & Pohlen, M. 2008, *ApJ*, 683, 403
- Barker, M. K., Sarajedini, A., Geisler, D., Harding, P., & Schommer, R. 2007, *AJ*, 133, 1125
- Beers, T. C. et al. 2005, in IAU Symp. 228, From Lithium to Uranium: Elemental Tracers of Early Cosmic Evolution, ed. V. Hill, P. François, & F. Primas (Dordrecht: Kluwer), 175
- Blair, W. P., & Long, K. S. 1997, *ApJS*, 108, 261
- Bland-Hawthorn, J., Vlahić, M., Freeman, K. C., & Draine, B. T. 2005, *ApJ*, 629, 239
- Boissier, S., & Prantzos, N. 1999, *MNRAS*, 307, 857
- Bresolin, F., Ryan-Weber, E., Kennicutt, R. C., & Goddard, Q. 2009, *ApJ*, 695, 580
- Brooks, R. S., Wilson, C. D., & Harris, W. E. 2004, *AJ*, 128, 237
- Bullock, J. S., & Johnston, K. V. 2005, *ApJ*, 635, 931
- Butler, D. J., Martínez-Delgado, D., & Brandner, W. 2004, *AJ*, 127, 1472
- Carignan, C. 1985, *ApJS*, 58, 107
- Carney, B. W., Yong, D., Teixeira de Almeida, M. L., & Seitzer, P. 2005, *AJ*, 130, 1111
- Carollo, D. et al. 2007, *Nature*, 450, 1020
- Chapman, S. C., Ibata, R., Lewis, G. F., Ferguson, A. M. N., Irwin, M., McConnachie, A., & Tanvir, N. 2006, *ApJ*, 653, 255
- Chen, L., Hou, J. L., & Wang, J. J. 2003, *AJ*, 125, 1397
- Chiappini, C., Matteucci, F., & Gratton, R. 1997, *ApJ*, 477, 765
- Chiappini, C., Matteucci, F., & Romano, D. 2001, *ApJ*, 554, 1044
- Collins, J. A., Shull, J. M., & Giroux, M. L. 2003, *ApJ*, 585, 336
- Collins, J. A., Shull, J. M., & Giroux, M. L. 2007, *ApJ*, 657, 271
- Daflon, S., & Cunha, K. 2004, *ApJ*, 617, 1115
- Davidge, T. J. 2003, *AJ*, 125, 3046
- Davidge, T. J. 2006, *ApJ*, 641, 822
- Davidge, T. J. 2007, *ApJ*, 664, 820
- de Grijs, R., Kregel, M., & Wesson, K. H. 2001, *MNRAS*, 324, 1074
- Dessauges-Zavadsky, M., Calura, F., Prochaska, J. X., D'Odorico, S., & Matteucci, F. 2004, *A&A*, 416, 79
- Dessauges-Zavadsky, M., Prochaska, J. X., D'Odorico, S., Calura, F., & Matteucci, F. 2006, *A&A*, 445, 93
- Ellis, S. C., & Bland-Hawthorn, J. 2007, *MNRAS*, 377, 815
- Erwin, P., Pohlen, M., Beckman, J. E., Gutierrez, L., & Aladro, R. 2008, in ASP Conf. Ser. 390, Pathways Through an Eclectic Universe, ed. J. H. Knapen, T. J. Mahoney, & A. Vazdekis (San Francisco, CA: ASP), 251
- Feltzing, S., & Gilmore, G. 2000, *A&A*, 355, 949
- Ferguson, A., Irwin, M., Chapman, S., Ibata, R., Lewis, G., & Tanvir, N. 2007, in Resolving the Stellar Outskirts of M31 and M33, ed. R. S. de Jong (Berlin: Springer), 239
- Ferguson, A. M. N., & Johnson, R. A. 2001, *ApJ*, 559, L13
- Freedman, W. L. et al. 2001, *ApJ*, 553, 47
- Freeman, K. C. 1970, *ApJ*, 160, 811
- Freeman, K., & Bland-Hawthorn, J. 2002, *ARA&A*, 40, 487
- Friel, E. D., Janes, K. A., Tavares, M., Scott, J., Katsanis, R., Lotz, J., Hong, L., & Miller, N. 2002, *AJ*, 124, 2693
- Frogel, J. A., Tiede, G. P., & Kuchinski, L. E. 1999, *AJ*, 117, 2296
- Fukugita, M., Ichikawa, T., Gunn, J. E., Doi, M., Shimasaku, K., & Schneider, D. P. 1996, *AJ*, 111, 1748
- Galletti, S., Bellazzini, M., & Ferraro, F. R. 2004, *A&A*, 423, 925
- Gieren, W. et al. 2004, *AJ*, 128, 1167
- Goetz, M., & Koeppen, J. 1992, *A&A*, 262, 455
- Hamann, F., & Ferland, G. 1999, *ARA&A*, 37, 487
- Harris, G. L. H., & Harris, W. E. 2000, *AJ*, 120, 2423
- Harris, G. L. H., Harris, W. E., & Poole, G. B. 1999, *AJ*, 117, 855
- Harris, W. E. 1996, *AJ*, 112, 1487
- Hook, I. M., Jørgensen, I., Allington-Smith, J. R., Davies, R. L., Metcalfe, N., Murowinski, R. G., & Crampton, D. 2004, *PASP*, 116, 425
- Hou, J. L., Prantzos, N., & Boissier, S. 2000, *A&A*, 362, 921
- Ibata, R., Chapman, S., Ferguson, A. M. N., Lewis, G., Irwin, M., & Tanvir, N. 2005, *ApJ*, 634, 287
- Ibata, R. A., Irwin, M. J., Lewis, G. F., Ferguson, A. M. N., & Tanvir, N. 2003, *MNRAS*, 340, L21
- Irwin, M. J., Ferguson, A. M. N., Ibata, R. A., Lewis, G. F., & Tanvir, N. R. 2005, *ApJ*, 628, L105
- Ivezic, Z., et al. 2008, *ApJ*, 684, 287
- Kennicutt, R. C., Jr. 1989, *ApJ*, 344, 685
- Kim, S. C., Sung, H., Park, H. S., & Sung, E.-C. 2004, *Chin. J. Astron. Astrophys.*, 4, 299
- Koch, A. et al. 2007, *Astron. Nachr.*, 328, 653
- Kudritzki, R., Urbaneja, M. A., Bresolin, F., Przybilla, N., Gieren, W., & Pietrzynski, G. 2008, *ApJ*, 681, 269
- Landolt, A. U. 1992, *AJ*, 104, 340
- Larson, R. B. 1976, *MNRAS*, 176, 31
- Maciel, W. J., Costa, R. D. D., & Uchida, M. M. M. 2003, *A&A*, 397, 667
- Maciel, W. J., Lago, L. G., & Costa, R. D. D. 2005, *A&A*, 433, 127
- Maciel, W. J., Lago, L. G., & Costa, R. D. D. 2006, *A&A*, 453, 587

- Maciel, W. J., Quireza, C., & Costa, R. D. D. 2007, [A&A](#), **463**, L13
- Matteucci, F., & Francois, P. 1989, *MNRAS*, **239**, 885
- McConnachie, A. W., Chapman, S. C., Ibata, R. A., Ferguson, A. M. N., Irwin, M. J., Lewis, G. F., Tanvir, N. R., & Martin, N. 2006, [ApJ](#), **647**, L25
- Metcalfe, N., Shanks, T., Campos, A., McCracken, H. J., & Fong, R. 2001, *MNRAS*, **323**, 795
- Minniti, D., Olszewski, E. W., Liebert, J., White, S. D. M., Hill, J. M., & Irwin, M. J. 1995, *MNRAS*, **277**, 1293
- Molla, M., Ferrini, F., & Diaz, A. I. 1997, [ApJ](#), **475**, 519
- Mouhcine, M., Rich, R. M., Ferguson, H. C., Brown, T. M., & Smith, T. E. 2005, [ApJ](#), **633**, 828
- Muñoz-Mateos, J. C., Gil de Paz, A., Boissier, S., Zamorano, J., Jarrett, T., Gallego, J., & Madore, B. F. 2007, [ApJ](#), **658**, 1006
- Naab, T., & Ostriker, J. P. 2006, *MNRAS*, **366**, 899
- Parmentier, G., Jehin, E., Magain, P., Noels, A., & Thoul, A. A. 2000, *A&A*, **363**, 526
- Pohlen, M., Dettmar, R.-J., Lütticke, R., & Aronica, G. 2002, *A&A*, **392**, 807
- Pohlen, M., Erwin, P., Trujillo, I., & Beckman, J. E. 2008, in ASP Conf. Ser. 390, Pathways Through an Eclectic Universe, ed. J. H. Knapen, T. J. Mahoney, & A. Vazdekis (San Francisco, CA: ASP), 247
- Portinari, L., & Chiosi, C. 1999, *A&A*, **350**, 827
- Prochaska, J. X., Gawiser, E., Wolfe, A. M., Castro, S., & Djorgovski, S. G. 2003, [ApJ](#), **595**, L9
- Puche, D., Carignan, C., & Bosma, A. 1990, *AJ*, **100**, 1468
- Quillen, A. C., Minchev, I., Bland-Hawthorn, J., & Haywood, M. 2009, [arXiv:0903.1851](#)
- Ramírez, S. V., Stephens, A. W., Frogel, J. A., & DePoy, D. L. 2000, *AJ*, **120**, 833
- Rich, R. M., Origlia, L., & Valenti, E. 2007, [ApJ](#), **665**, L119
- Robin, A. C., Reylé, C., Derrière, S., & Picaud, S. 2003, *A&A*, **409**, 523
- Roškar, R., Debattista, V. P., Stinson, G. S., Quinn, T. R., Kaufmann, T., & Wadsley, J. 2008a, [ApJ](#), **675**, L65
- Roškar, R., Debattista, V. P., Quinn, T. R., Stinson, G. S., & Wadsley, J. 2008b, [ApJ](#), **684**, L79
- Saviane, I., Rosenberg, A., Piotto, G., & Aparicio, A. 2000, *A&A*, **355**, 966
- Schaye, J. 2004, [ApJ](#), **609**, 667
- Schlegel, D. J., Finkbeiner, D. P., & Davis, M. 1998, [ApJ](#), **500**, 525
- Schoenrich, R., & Binney, J. 2008, [arXiv:0809.3006](#)
- Sellwood, J. A., & Binney, J. J. 2002, *MNRAS*, **336**, 785
- Sellwood, J. A., & Preto, M. 2002, in ASP Conf. Ser. 275, Disks of Galaxies: Kinematics, Dynamics and Perturbations, ed. E. Athanassoula, A. Bosma, & R. Muijca (San Francisco, CA: ASP), 281
- Stetson, P. B. 1987, *PASP*, **99**, 191
- Stetson, P. B. 1990, *PASP*, **102**, 932
- Stetson, P. B., & Harris, W. E. 1988, *AJ*, **96**, 909
- Tikhonov, N. A., Galazutdinova, O. A., & Drozdovsky, I. O. 2005, *A&A*, **431**, 127
- Tosi, M. 1988, *A&A*, **197**, 47
- Twarog, B. A., Ashman, K. M., & Anthony-Twarog, B. J. 1997, *AJ*, **114**, 2556
- Urbaneja, M. A. et al. 2005, [ApJ](#), **622**, 862
- van der Kruit, P. C. 1979, *A&AS*, **38**, 15
- van der Kruit, P. C. 2007, *A&A*, **466**, 883
- VandenBerg, D. A., Bergbusch, P. A., & Dowler, P. D. 2006, *ApJS*, **162**, 375
- Wolfe, A. M., Gawiser, E., & Prochaska, J. X. 2005, *ARA&A*, **43**, 861
- Worthey, G., España, A., MacArthur, L. A., & Courteau, S. 2005, [ApJ](#), **631**, 820
- Yong, D., Carney, B. W., & Teixeira de Almeida, M. L. 2005, *AJ*, **130**, 597
- Yong, D., Carney, B. W., Teixeira de Almeida, M. L., & Pohl, B. L. 2006, *AJ*, **131**, 2256
- Younger, J. D., Cox, T. J., Seth, A. C., & Hernquist, L. 2007, [ApJ](#), **670**, 269
- Zoccali, M., Hill, V., Lecureur, A., Barbuy, B., Renzini, A., Minniti, D., Gomez, A., & Ortolani, S. 2008, *A&A*, **486**, 177